

# Controllable growth of layered selenide and telluride heterostructures and superlattices using molecular beam epitaxy

Suresh Vishwanath<sup>a)</sup>

*School of Electrical and Computer Engineering, Cornell University, Ithaca, New York 14853, USA; and Department of Electrical Engineering, University of Notre Dame, Notre Dame, Indiana 46556, USA*

Xinyu Liu

*Department of Physics, University of Notre Dame, Notre Dame, Indiana 46556, USA*

Sergei Rouvimov

*Department of Electrical Engineering, University of Notre Dame, Notre Dame, Indiana 46556, USA*

Leonardo Basile

*Departamento de Física, Escuela Politécnica Nacional, Quito 170525, Ecuador; and Oak Ridge National Laboratory, Center of Nanophase Materials Sciences, Oak Ridge, Tennessee 37831, USA*

Ning Lu and Angelica Azcatl

*Department of Materials Science and Engineering, University of Texas at Dallas, Richardson, Texas 75083, USA*

Katrina Magno

*Department of Physics, University of Notre Dame, Notre Dame, Indiana 46556, USA*

Robert M. Wallace and Moon Kim

*Department of Materials Science and Engineering, University of Texas at Dallas, Richardson, Texas 75083, USA*

Juan-Carlos Idrobo

*Center of Nanophase Materials Sciences, Oak Ridge, Tennessee 37831, USA*

Jacek K. Furdyna

*Department of Physics, University of Notre Dame, Notre Dame, Indiana 46556, USA*

Debdeep Jena and Huili Grace Xing<sup>b)</sup>

*School of Electrical and Computer Engineering, Cornell University, Ithaca, New York 14853, USA; Department of Electrical Engineering, University of Notre Dame, Notre Dame, Indiana 46556, USA; and Department of Materials Science and Engineering, Cornell University, Ithaca, New York 14853, USA*

(Received 11 October 2015; accepted 23 November 2015)

Layered materials are an actively pursued area of research for realizing highly scaled technologies involving both traditional device structures as well as new physics. Lately, non-equilibrium growth of 2D materials using molecular beam epitaxy (MBE) is gathering traction in the scientific community and here we aim to highlight one of its strengths, growth of abrupt heterostructures, and superlattices (SLs). In this work we present several of the firsts: first growth of MoTe<sub>2</sub> by MBE, MoSe<sub>2</sub> on Bi<sub>2</sub>Se<sub>3</sub> SLs, transition metal dichalcogenide (TMD) SLs, and lateral junction between a quintuple atomic layer of Bi<sub>2</sub>Te<sub>3</sub> and a triple atomic layer of MoTe<sub>2</sub>. Reflected high electron energy diffraction oscillations presented during the growth of TMD SLs strengthen our claim that ultrathin heterostructures with monolayer layer control is within reach.

## I. INTRODUCTION

Discovery of graphene<sup>1</sup> led to renewed interest in layered transition metal dichalcogenides (TMDs) like MoS<sub>2</sub>, ReSe<sub>2</sub>, WSe<sub>2</sub> and MoTe<sub>2</sub> as well as post-TMDs like InSe, GaSe, and SnSe<sub>2</sub> (Refs. 2–5) for electronic as well as optical devices. Quasi-two dimensional (2D) materials like Bi<sub>2</sub>Te<sub>3</sub>, Bi<sub>2</sub>Se<sub>3</sub>, and Sb<sub>2</sub>Te<sub>3</sub> are of great

scientific interest as topological insulators as well as thermoelectric materials.<sup>6,7</sup> Recently, there has been an enormous number of reports of optical and electronic devices involving different 2D materials and their heterostructures either exfoliated<sup>8–11</sup> or chemical vapor deposition (CVD) grown.<sup>12–15</sup> Quasi-2D material superlattices (SLs) have been shown to have superior thermoelectric properties.<sup>16,17</sup> Molecular beam epitaxy (MBE) of 2D materials although pioneered in early 1990s<sup>18–22</sup> has been dormant until recently.<sup>23–29</sup> Historically, strength of MBE is growth of abrupt heterostructures at lower temperatures, alloying, delta doping, and in situ monitoring of growth for monolayer control. Geim,

Contributing Editor: Jeremy T. Robinson  
Address all correspondence to these authors.

<sup>a)</sup>e-mail: sv372@cornell.edu

<sup>b)</sup>e-mail: grace.xing@cornell.edu

DOI: 10.1557/jmr.2015.374

in his paper on van der Waals heterostructures,<sup>30</sup> proposes a dreamscape for 2D materials where they can be stacked as lego blocks to realize various structures desirable to probe novel physics and device applications.<sup>31</sup> In this report we aim to show that we are a step closer to achieving that dreamscape using MBE for growing 2D and quasi-2D materials.

Heterostructures and SLs in 3D materials have opened doors for a myriad of high performance devices like heterojunction bipolar transistors,<sup>32,33</sup> multi quantum well lasers,<sup>34</sup> etc; also SLs drive home the claim that these materials can be used as lego blocks. Also, this is the first report where MBE growth of MoTe<sub>2</sub> has been demonstrated. Due to weak bonding between Mo and arising from similar electronegativity,<sup>35</sup> it has been hard to obtain MoTe<sub>2</sub> using CVD. MoTe<sub>2</sub> has been obtained using tellurization of e-beam deposited molybdenum films<sup>36</sup> and bulk crystals by chemical vapor transport (CVT). CVT process involves use of a transport agent and also the transporting agent, usually a halogen, gets incorporated into the crystal. This incorporation is close to 1 % of the CVT grown crystal by weight, which is a very high unintentional doping from a device perspective.<sup>37</sup> This is evident from the fact that MoTe<sub>2</sub> grown using Te as the transport agent is p-type but when grown using Br it is n-type.<sup>38</sup>

In a 3D semiconductor system, the growth of heterostructures is limited primarily by the lattice mismatch between various layers. Hence, a figure like Fig. 1(a) plotting band gap versus lattice constant sets the constraints on choice of layers in a heterostructure and the growth substrate. But in case of a layered material grown on a layered material, as we had reported in the case of MBE MoSe<sub>2</sub> grown on graphene and highly ordered pyrolytic graphite (HOPG)<sup>24</sup>; we observe superimposed reflected high electron energy diffraction (RHEED) signals from the underlying substrate and the as grown film in case of an incomplete coverage. This suggests that the growth of 2D materials is by van der Waals epitaxy. This is supported by the fact we do not see any discernable change in lattice constants in monolayers as one moves away from the interface in aberration-corrected scanning transmission electron microscopy (STEM) images shown further below. This gives us an added freedom to design electronic or optical devices solely using the desired band alignments as shown in Fig. 1(b). Promise of few-layer heterostructures has been demonstrated in form of WSe<sub>2</sub>/MoS<sub>2</sub> p-n junctions,<sup>39</sup> black phosphorus/SnSe<sub>2</sub> tunnel diodes.<sup>40</sup> Near broken band alignment for WSe<sub>2</sub>/SnSe<sub>2</sub>, MoTe<sub>2</sub>/SnSe<sub>2</sub>, GaSe/SnSe<sub>2</sub> seen in Fig. 1(b) is very interesting for electronic applications like highly scaled tunnel field effect transistors (Thin-TFET).<sup>41</sup> With the recent observation of direct band gap in few layer MoTe<sub>2</sub> (Ref. 42) and in bulk ReS<sub>2</sub>,<sup>43</sup> few layered materials and heterostructures would likely be in limelight for optoelectronic devices as well.

2D and quasi-2D materials don't yet have uniformly accepted definitions. For this work, we have used the Fig. 1(c), where we plot the lattice constant perpendicular to the cleavage plane of the layered material divided by the sum of the ionic radii of the constituent atoms of the monolayer versus the number of atomic layers comprising the monolayer, to differentiate the two classes of materials among layered materials with multiple atomic layers per monolayer. We see that for layered materials having 3 atomic layers in a monolayer, all materials irrespective of the group in the periodic table to which the cation belongs are clustered together. Whereas in 2 atomic layers or 5 atomic layers, the ratio changes dramatically with change in the group to which the cation belongs. The definition holds good for layered materials having greater than one atomic layer per monolayer. It gives us a rough estimate of the fraction van der Waals gap per monolayer height. Hence, in spite of the quasi-2D materials being layered, the cation in one monolayer likely has more significant interaction with the cation in the next monolayer when compared to 2D materials.

It is finally important to stress that MBE is capable of producing monolayer materials<sup>25</sup> and their heterostructures but the growth to date is not self-limiting and hence it needs to be timed using RHEED intensity oscillations. This doesn't give perfect monolayer control as discussed further. Hence, the focus is on few layer SLs and heterostructure in this paper.

## II. IN SITU GROWTH OF TMD (MoTe<sub>2</sub>/MoSe<sub>2</sub>) SL

This is the first demonstration of in situ growth of 2D material SLs. As shown in Fig. 2, we demonstrate an MBE MoSe<sub>2</sub>/MoTe<sub>2</sub> SL on GaAs (111)B substrates. GaAs substrate was chosen as high quality epi ready GaAs substrates are commercially available and the surface can be made quasi-van der Waals employing a surface termination with chalcogen atoms. Replacement of surface arsenic with sulfur retaining 1 × 1 reconstruction has been observed in GaAs (111) immersed in NH<sub>4</sub>S solution<sup>44</sup> and such sulfur terminated GaAs has been previously used for MBE growth of layered materials like MoSe<sub>2</sub>.<sup>45</sup> In this work, we deoxidize GaAs in situ (at a thermocouple temperature of 730 °C) and then anneal under a Te flux for 5 min, followed by cool down to the growth temperature of 380 °C (thermocouple temperature). The effect of this tellurium treatment is shown in Fig. 3. When the surface is just deoxidized without Te treatment [Fig. 3(a)], the surface is heavily pitted with ~10 nm deep triangular craters, which results in a broken RHEED pattern from the surface. When the surface treatment is performed [Fig. 3(b)], the surface becomes much smoother showing wider and shallower triangles, which are most likely GaAs/Te islands with atomic step heights as shown in Fig. 2(f). Correspondingly, the

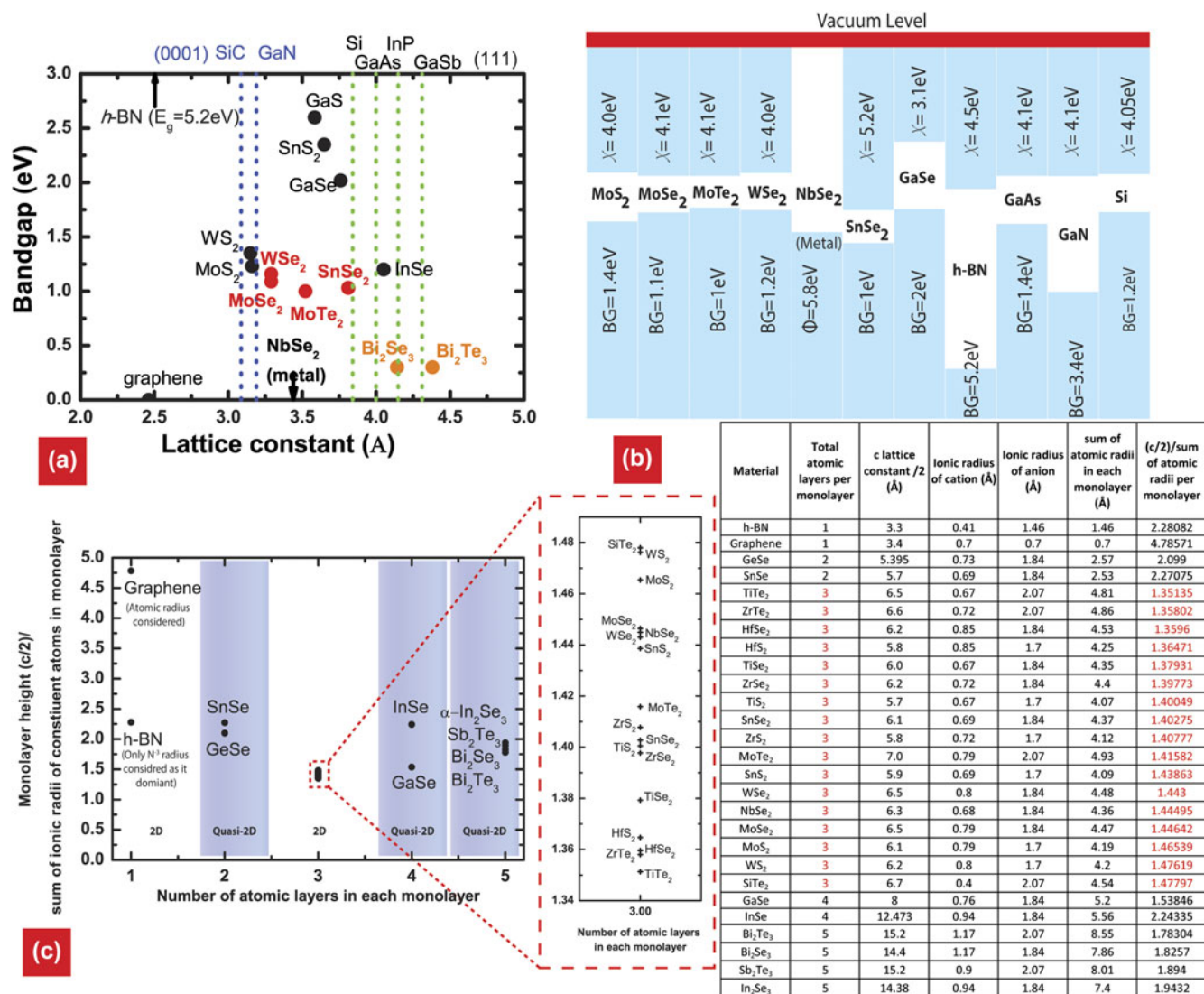


FIG. 1. (a) Plot showing band gap versus lattice constant of various bulk layered materials. Materials in red are the layered 2D materials of interest in this work, in orange are the quasi-2D layered materials presented here, blue lines represent the lattice constant of common bulk 3D substrates with hexagonal symmetry and green lines those with cubic symmetry (<http://www.ioffe.ru/>). (b) Cumulative plot of experimentally determined<sup>20</sup> band gaps (BG) and electron affinity ( $X$ ) of various layered materials in bulk form, contrasted to common compound semiconductor substrates. (c) The monolayer height [half of the lattice constant perpendicular to the cleavage plane of a bulk crystal ( $c/2$ )] divided by the sum of the ionic radii (atomic radii in case of graphene) of constituent atoms in each monolayer is plotted against the number of atomic layers in each monolayer.

RHEED patterns become sharp and streaky as in Fig. 2(d). This shows that there are atomic motions on the surface assisted by Te atoms. Furthermore, the high angle annular dark field-scanning transmission electron microscope (HAADF-STEM) image in Fig. 2(f) shows the very top row of the As–Ga atomic pair of the GaAs substrate appears brighter than the As–Ga pairs below, strengthening the claim of Te replacing As on the GaAs surface.

As shown in the growth diagram in Fig. 2(a), once the substrate is cooled down to the growth temperature and stabilized, Mo and Te molecular beams are simultaneously incident on the substrate. The Mo molecular beam is from an e-beam source and Te and Se are from Kundsens cells. All the data presented in Fig. 2, except for

the RHEED oscillations, are for a growth with 480 s for each period. The Mo flux is kept constant and the Te and Se fluxes are alternated. The key point drawn from Fig. 2(b) is that Raman from the SL is superposition of Raman from both MoSe<sub>2</sub> and MoTe<sub>2</sub>, which is expected but it is interesting to note that the Raman efficiency from MoTe<sub>2</sub> is much lower than that from MoSe<sub>2</sub>. Also, as some of the Raman peaks were masked by peaks from the longitudinal optical (LO) and transverse optical (TO) phonons in GaAs,<sup>46</sup> the MoTe<sub>2</sub>/MoSe<sub>2</sub> SL was exfoliated onto a SiO<sub>2</sub>/Si substrate and Raman was carried out to confirm the peaks. Raman spectroscopy, measured using a 488 nm laser, an incident power of 633  $\mu$ W and averaged over several scans, shows

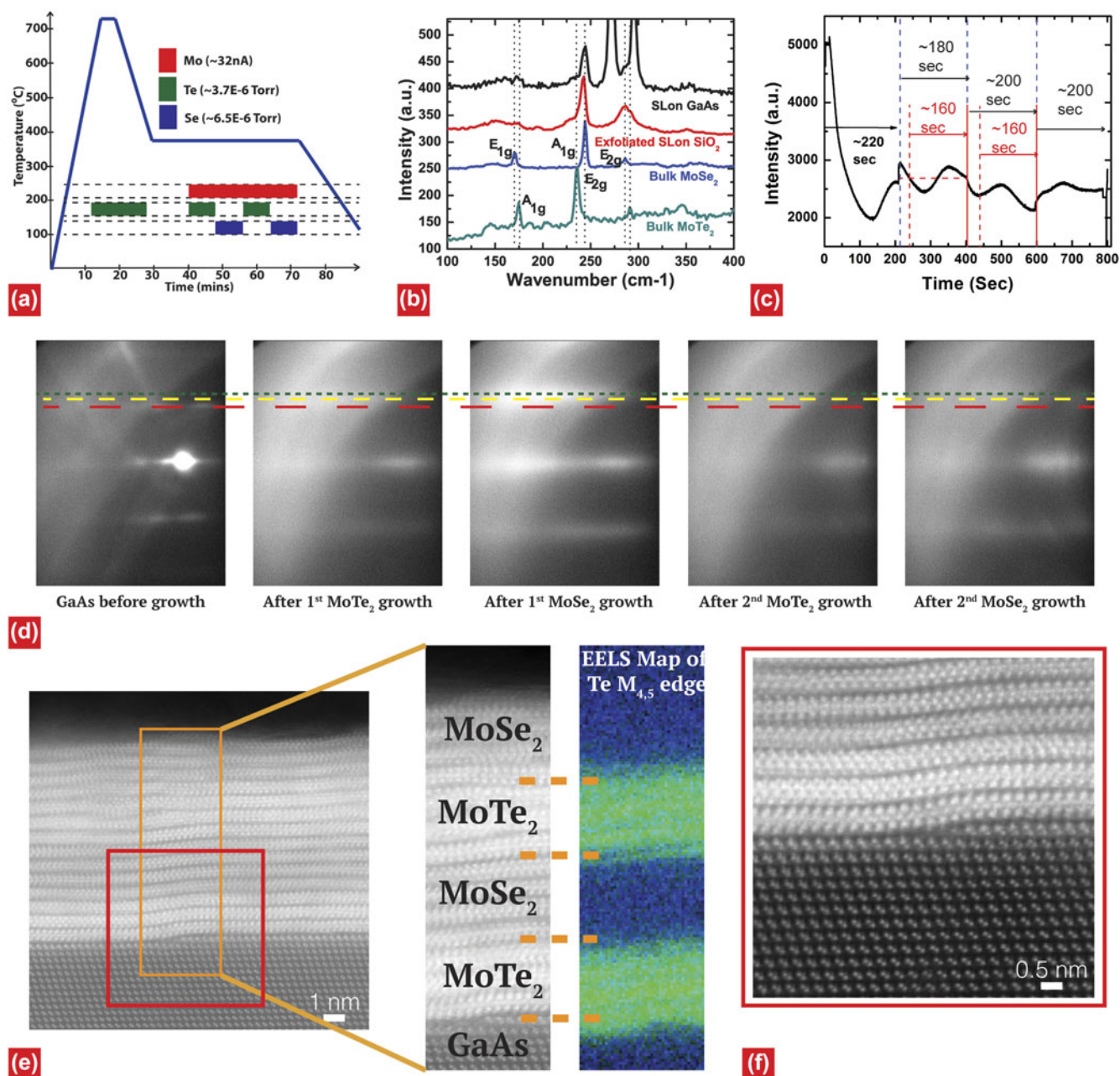


FIG. 2. (a) Growth diagram of the  $\text{MoTe}_2/\text{MoSe}_2$  SL on GaAs (111)B. (b) Raman from the SL (on GaAs as well as exfoliated onto  $\text{SiO}_2/\text{Si}$ ) compared to Raman signal from CVT grown bulk  $\text{MoSe}_2$  and bulk  $\text{MoTe}_2$ . (c) RHEED oscillation from a sample grown under the same condition but for a shorter duration for each period. Blue lines show where the chalcogen is switched and the dashed red line to the solid red line mark one period of the oscillation. (d) Evolution of RHEED signal from the sample shown in Fig. 2(c), RHEED streaks from GaAs are superimposed by the red line,  $\text{MoTe}_2$  in yellow and  $\text{MoSe}_2$  in green. (e) HAADF-STEM image of the SL and EELS map of Te  $M_{4,5}$  edge, which clearly shows abruptness of different layers. (f) Higher magnification image of the red box in Fig. 2(e) showing how  $\text{MoTe}_2$  climbs over an atomic step on GaAs.

a  $\text{MoSe}_2$   $A_{1g}$  peak at  $242.02 \text{ cm}^{-1}$  and  $E_{2g}$  peak at  $286.3 \text{ cm}^{-1}$ , which is consistent with the observations on MBE grown  $\text{MoSe}_2$  on HOPG.<sup>24</sup> The  $E_{2g}$  peak seems to comprise of 2 very close peaks, one from  $\text{MoSe}_2$  and one from  $\text{MoTe}_2$ . Figure 2(d) shows the RHEED evolution along the growth of the SL. It can be clearly seen that the RHEED streak spacing is inverse of the lattice spacing

shown in Fig. 1(a). The ratio of the inverse of the RHEED streak spacing closely matches the ratio of reported lattice spacing.<sup>47</sup> The ratio of the lattice spacing of (111) GaAs:  $\text{MoTe}_2:\text{MoSe}_2$  from the literature is  $3.997 (a_{\text{GaAs}}/\sqrt{2}):3.522:3.299$  (where "a" is lattice constant of GaAs), which is equivalently 1:0.88:0.82. The ratio of the inverse of RHEED streak spacing of the Red, Yellow, and Green

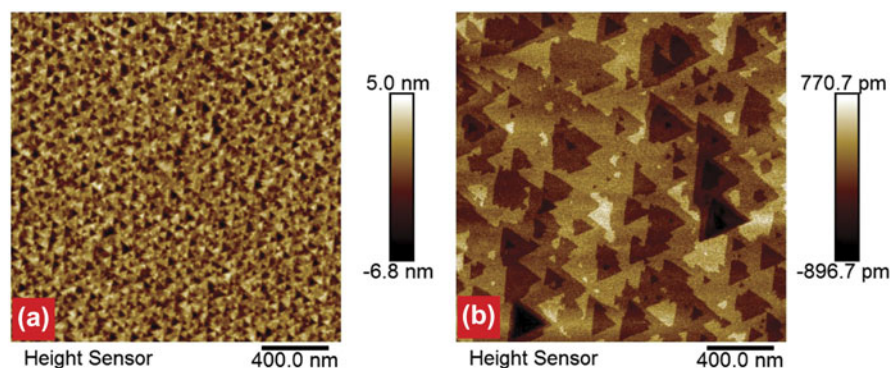


FIG. 3. AFM images of (a) deoxidized GaAs surface without tellurium treatment, and (b) deoxidized GaAs surface followed by Te treatment.

lines is 1:0.88:0.81, which is within the error margin given the RHEED patterns from the TMD layers are diffused.

It is also interesting to note that starting from the second  $\text{MoTe}_2$  layer polycrystalline ring develops along with the streaky RHEED. This is correlated with the waviness in the  $\text{MoTe}_2$  in the 2nd period of the SL and  $\text{MoSe}_2$  in the 2nd period of the SL as seen from the cross-sectional HAADF-STEM image in Fig. 2(e). This polycrystallinity deteriorates RHEED oscillations, therefore, the RHEED oscillation presented in Fig. 2(c) is from a different growth under the same growth condition but with thinner layers, which was used to calibrate the growth rate. Since Mo is a refractory metal and the substrate temperature is low, the sticking coefficient of Mo can be safely assumed to be 1 at the surface thus the growth rate is limited by the Mo deposition rate. The RHEED oscillation period is taken to be the duration of one monolayer. From the 2nd and 3rd oscillation in Fig. 2(c), one oscillation period (duration between the dashed red line and the solid red line) can be estimated to be  $\sim 160$  s, i.e., a growth rate of 1 monolayer per 160 s. In the 2nd oscillation, it is taken as double of the duration between the minimum and maximum. In the 3rd oscillation, as the duration between the 2 minima. It is an approximation since, Mo flux from e-beam changes slightly between growths and during growth itself. Based on this observation, each half-period of the reported SL growth in Fig. 2(e) is carried out for 480 s, which corresponds to 3 monolayers. However, it is worth noting that in the region in Fig. 2(e) marked by an orange box we can see that there are 3 monolayers of  $\text{MoTe}_2$  and 4 monolayers of  $\text{MoSe}_2$  in the 1st period, and there are 4 layers of  $\text{MoTe}_2$  and  $\text{MoSe}_2$  in the 2nd period. Together with the substrate surface features of atomic heights, this suggests that observation of RHEED oscillation doesn't necessarily mean a full layer-by-layer growth. In fact, delay in the RHEED intensity and oscillation magnitude is a result of cumulative interference from a roughening film. In spite of that during growth the Se and Te flux is

about 3 orders magnitude higher than the Mo flux and there are no breaks between the Se pulse and Te pulse to remove excess Se or Te from the surface, very abrupt  $\text{MoTe}_2$  and  $\text{MoSe}_2$  interfaces have been achieved. This is evidenced by the atomic resolution electron energy loss spectroscopy (EELS) map of the Te  $M_{4,5}$  edge of the SL. The sharpness of the map is demonstrated by the fact that the Te signal takes a bend over the GaAs step where the layers bend. Figure 2(f) shows how the  $\text{MoTe}_2$  layers climb over an atomic step on GaAs and that there is no chemical bond between the 2D material and the 3D substrate treated with Te.

### III. IN SITU GROWTH OF TMD/QUASI-2D CRYSTAL ( $\text{MoX}_2/\text{Bi}_2\text{X}_3$ ) SL

Diced sapphire substrates were first cleaned sequentially in chloroform (30 min), acetone (15 min), methanol (5 min), and hydrofluoric acid (HF) (10%, 2 min). The substrate was then loaded into the MBE chamber, heated to 800 °C and held for 30 min, then cooled to 200 °C. Once the temperature was stabilized the first 2–3 monolayers of  $\text{Bi}_2\text{X}_3$  (X denotes Se or Te) was deposited. RHEED from sapphire is observed to disappear; when the substrate is heated gradually to the growth condition of 340 °C (avoiding any overshoot), the  $\text{Bi}_2\text{X}_3$  RHEED pattern appears. This is similar to the growth reported for  $\text{Bi}_2\text{X}_3$  on GaAs (001).<sup>48</sup> Subsequently, the  $\text{Bi}_2\text{X}_3$  and  $\text{MoX}_2$  SL was grown. The reason for this increase in Te flux before  $\text{MoTe}_2$  growth on  $\text{Bi}_2\text{Te}_3$  is presented elsewhere.<sup>49</sup>

Figures 4(b) and 5(b) shows that Raman from the SL is a superimposition from individual components of respective SLs,  $\text{Bi}_2\text{Te}_3/\text{MoTe}_2$  and  $\text{Bi}_2\text{Se}_3/\text{MoSe}_2$ . Again, even though in both SLs the thickness of  $\text{MoX}_2$  is almost equal, the Raman signal from  $\text{MoTe}_2$  is much lower and broader than from  $\text{MoSe}_2$ , which is consistent with the observation in the  $\text{MoTe}_2/\text{MoSe}_2$  SL (Fig. 2). The  $\text{MoTe}_2$   $A_{1g}$  peak at  $\sim 171$   $\text{cm}^{-1}$  and  $E_{2g}$  at  $\sim 230$   $\text{cm}^{-1}$  (obtained

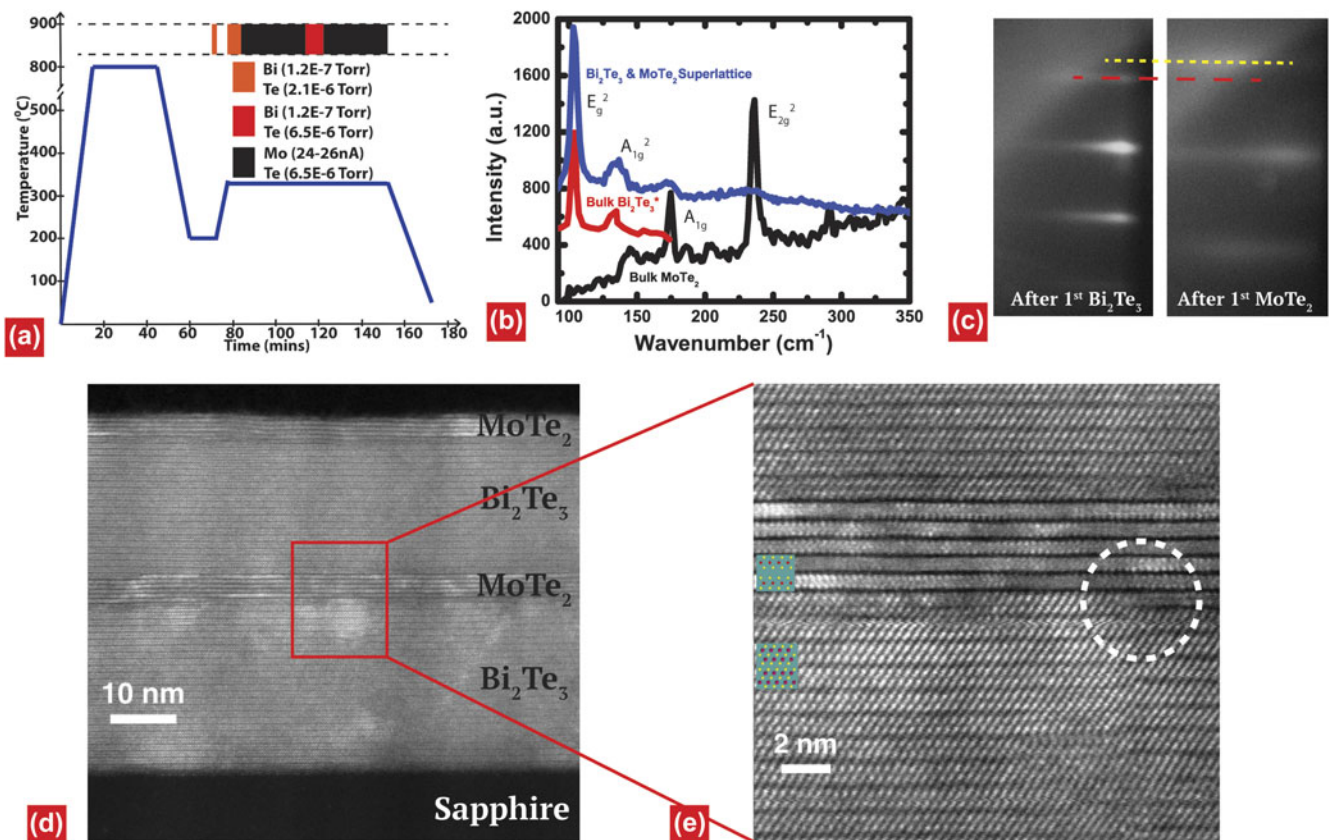


FIG. 4. (a) Growth diagram of the Bi<sub>2</sub>Te<sub>3</sub>/MoTe<sub>2</sub> SL, (b) Raman spectrum from the SL compared to that from bulk MoTe<sub>2</sub> and the \*reported spectrum<sup>50</sup> for bulk Bi<sub>2</sub>Te<sub>3</sub>, (c) RHEED showing that MoTe<sub>2</sub> has a smaller lattice constant than Bi<sub>2</sub>Te<sub>3</sub> hence the reverse in the reciprocal space, (d) HAADF-STEM image of the SL showing the abruptness of different materials, (e) higher magnification image of the red box in Fig. 4(d) showing that the lattice constant of the 2 materials is consistent with that of the bulk and how a MoTe<sub>2</sub> layer stitches to a partial layer of Bi<sub>2</sub>Te<sub>3</sub>.

by Lorentz fitting to the broad peaks) can be better resolved due to the absence of MoSe<sub>2</sub> Raman peaks in the neighborhood, which are close to the values from bulk MoTe<sub>2</sub> at 174.4 and 235.8 cm<sup>-1</sup>. 1T-MoTe<sub>2</sub> has been reported to have very different peak positions from 2H-MoTe<sub>2</sub>,<sup>36</sup> therefore, this observed shift and broadening in MoTe<sub>2</sub> peaks are more likely due to the small grain size in the MBE grown MoTe<sub>2</sub> as compared to the bulk. We assume there is no systematic zero error since the E<sub>2g</sub> peak of Bi<sub>2</sub>Te<sub>3</sub> is at 103.8 cm<sup>-1</sup> and the A<sub>1g</sub><sup>2</sup> peak is at 134.7 cm<sup>-1</sup>, consistent with the reported values for bulk Bi<sub>2</sub>Te<sub>3</sub>.<sup>50,51</sup> The bulk value measured by us is consistent with the reported value for bulk 2H-MoTe<sub>2</sub>.<sup>52</sup> RHEED in Fig. 4(c) is in line with the expectation that Bi<sub>2</sub>Te<sub>3</sub> has a wider lattice spacing than MoTe<sub>2</sub> hence a narrower spacing in the reciprocal space. It is worth noting that RHEED from MoTe<sub>2</sub> is much more diffused than that from Bi<sub>2</sub>Te<sub>3</sub>, pointing toward a greater disorder and smaller grains in MoTe<sub>2</sub>. This is similar to the small grains reported in MBE MoSe<sub>2</sub> on graphene,<sup>24,25</sup> owing to the low adatom surface diffusivity of refractory metals. Bi<sub>2</sub>Te<sub>3</sub> RHEED sharpness recovers during the subsequent growth on MoTe<sub>2</sub>, adding strength to the above claim.

The most interesting observation in transmission electron microscopy (TEM) imaging of this SL sample is that a lateral junction between a quintuple layer Bi<sub>2</sub>Te<sub>3</sub> and a trilayer MoTe<sub>2</sub> is seen, shown in Fig. 4(e). This is the first ever observation of a lateral junction between a quasi-2D layer and a 2D layer. We see that the top 3 layers of the Quintuple (Te–Bi–Te) transition into (Te–Mo–Te). Such a junction might open paths for novel devices not envisioned before involving structurally different layered materials.

A substrate temperature of 340 °C was chosen to grow the Bi<sub>2</sub>X<sub>3</sub>/MoX<sub>2</sub> SL samples presented in Figs. 4 and 5 (a)–5(d) since the growth of Bi<sub>2</sub>X<sub>3</sub> was optimized near 340 °C. In our previous work MBE growth of MoSe<sub>2</sub> was carried out at a substrate temperature of 400 °C. To explore the effects of the substrate temperature, growths of MoSe<sub>2</sub> at 340 and 400 °C were carried out on Bi<sub>2</sub>Se<sub>3</sub>, which was grown on sapphire at 340 °C as described previously. In case of MoSe<sub>2</sub> growth at 400 °C, the first layer of MoSe<sub>2</sub> was grown at 340 °C and then substrate was heated to 400 °C for subsequent layers to avoid any dissociation of Bi<sub>2</sub>Se<sub>3</sub>. Atomic force microscopy (AFM) imaging of the as grown Bi<sub>2</sub>Se<sub>3</sub> at 340 °C [Fig. 5(g)]

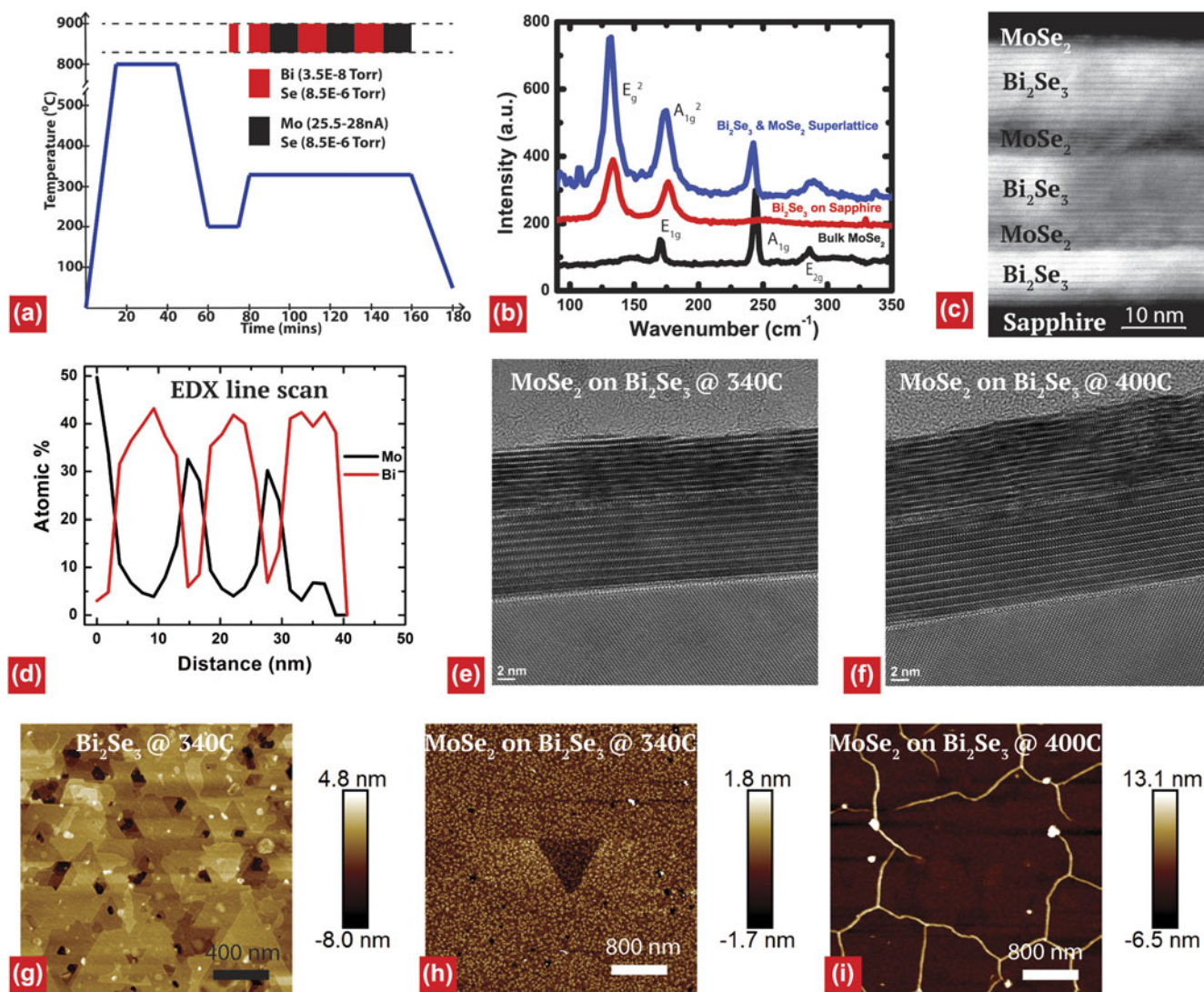


FIG. 5. (a) Growth diagram of the  $\text{Bi}_2\text{Se}_3/\text{MoSe}_2$  SL, (b) Raman spectra from the SL compared to that from bulk  $\text{MoSe}_2$  and MBE grown  $\text{Bi}_2\text{Se}_3$  on sapphire, (c) HAADF-STEM image of the SL, (d) EDX line scan of the SL showing abruptness of the Mo and Bi species, the widening of the edge is due to sample motion during imaging, (e) high-resolution transmission electron microscopy (HRTEM) of  $\text{MoSe}_2$  grown at 340 °C on  $\text{Bi}_2\text{Se}_3$ , the same growth condition as the SL, (f) HRTEM of  $\text{MoSe}_2$  grown at 400 °C on  $\text{Bi}_2\text{Se}_3$ , the same growth condition as the SL, (g) AFM of  $\text{Bi}_2\text{Se}_3$  grown on sapphire at 340 °C, the same growth condition as the first layer in the SL, (h) AFM of  $\text{MoSe}_2$  grown at 340 °C [sample in Fig. 5(e)], and (i) AFM of  $\text{MoSe}_2$  grown at 400 °C [sample in Fig. 5(f)].

shows triangular domains consistent with other reports.<sup>48</sup> When AFM images from  $\text{MoSe}_2$  growth at 340 °C [Fig. 5 (h)] are contrasted to those at 400 °C [Fig. 5(i)], significant differences in surface morphology are observed. The  $\text{MoSe}_2$  at 340 °C follows the contours of the underlying  $\text{Bi}_2\text{Se}_3$  and hence any pits in  $\text{Bi}_2\text{Se}_3$  are also seen after growth of  $\text{MoSe}_2$ . But when the growth is done at 400 °C we observe features similar to that observed on thick MBE  $\text{MoSe}_2$  on HOPG,<sup>24</sup> i.e., tall protrusions enclosing large smooth regions. TEM imaging of the 2 samples [Figs. 5(e) and 5 (f)] reveals that  $\text{MoSe}_2$  grown at 400 °C has a greater waviness but the interface between  $\text{Bi}_2\text{Se}_3$  and  $\text{MoSe}_2$  is sharp in both cases. Further investigations are necessary to understand the exact mechanisms behind these observations.

Finally, energy dispersive x-ray spectrum (EDX) line scan shown in Fig. 5(d) is consistent with the expected 40% Bi in  $\text{Bi}_2\text{Se}_3$  and 33.3% Mo expected in  $\text{MoSe}_2$ . Local variations in the height of  $\text{Bi}_2\text{Se}_3$  triangular grain along the width of the TEM sample and slight sample drift during the scan likely contribute to the overlap in the Bi and Mo signals in contrast to the sharp interface in HAADF-STEM [Fig. 5(c)].

#### IV. IN SITU GROWTH OF HETEROSTRUCTURES INVOLVING MORE THAN 3 MATERIALS

We have grown layered crystals ( $\text{MoSe}_2$ ,  $\text{MoTe}_2$ ,  $\text{SnSe}_2$ ,  $\text{WSe}_2$ ) on a 3D substrate ( $\text{GaAs}$ ,  $\text{CaF}_2$ ) and

quasi-2D crystals ( $\text{Bi}_2\text{Se}_3$ ,  $\text{Bi}_2\text{Se}_3$ ) with very small band gaps ( $\sim 200$  meV), and growth of quasi-2D materials like SnSe ( $\sim 0.86$  eV bulk indirect band gap)<sup>50</sup> and GaSe on a 2D substrate is equally interesting. Of particular interest is the Sn–Se system, because SnSe has been shown to have exceptional thermoelectric properties<sup>53</sup> and SnSe<sub>2</sub> is a layered material with high work function ideal for tunnel junctions. Monolayer and few layer SnSe has only been demonstrated to date using solution synthesis.<sup>54</sup> Taking guidelines from previously reported growth conditions for MBE growth of SnSe and SnSe<sub>2</sub> on layered materials<sup>55,56</sup> we grew a heterostructure involving 3 materials:  $\text{Bi}_2\text{Se}_3$ ,  $\text{MoSe}_2$ , and SnSe<sub>2</sub>. The corresponding growth diagram is shown in Fig. 6(a). Raman measurements show superimposition of expected layered materials. The shift of SnSe<sub>2</sub> peaks is likely due to difference in stacking order of bulk SnSe<sub>2</sub> and MBE SnSe<sub>2</sub>.<sup>57–59</sup> The cross-sectional TEM [Fig. 6(c)] image reveals that majority of the deposited Sn–Se was in form of SnSe<sub>2</sub>, but there were some regions of SnSe. What is very interesting is that a band of SnSe forms at the interface between  $\text{MoSe}_2$  and SnSe<sub>2</sub>. Our hypothesis is that even though the growth temperature was lowered from 340 to 240 °C for the growth of SnSe<sub>2</sub>, the growth temperature of 240 °C wasn't stabilized for long enough, essentially resulting in a higher than desired growth temperature for

the first few layers. Indeed we have consistently observed that SnSe grows at a higher temperature than SnSe<sub>2</sub>. While a separate manuscript<sup>59</sup> is under preparation to report the MBE growth of SnSe and SnSe<sub>2</sub>, we present here two sets of growth. Samples in Fig. 6(d) (SnSe<sub>x</sub> grown at 240 °C on MBE  $\text{MoSe}_2/\text{Bi}_2\text{Se}_3/\text{Sapphire}$ ) and Fig. 6(e) [SnSe grown at 240 °C on exfoliated  $\text{MoS}_2/\text{SiO}_2$  (300 nm)/Si] differ primarily by substrate alone. Samples in Figs. 6(e) and 6(f) [SnSe<sub>2</sub> grown at 200 °C on exfoliated  $\text{WSe}_2/\text{SiO}_2$  (300 nm)/Si] differ primarily by growth temperature. Although using STEM imaging only SnSe is seen on exfoliated  $\text{MoS}_2$  in Fig. 6(e), in order to see if there is SnSe<sub>2</sub> in other regions of the film, X-ray photoelectron spectroscopy (XPS) was performed on the sample. In agreement with the STEM imaging, the XPS spectra for Fig. 6(e) shows that majority of the as grown film is indeed comprised of the SnSe phase, at a binding energy of 54.3 eV in Se 3d and 485.5 eV in Sn 3d, which are consistent with the values reported in literature.<sup>60</sup> Yet, in addition to this phase, a small but significant amount of SnSe<sub>2</sub> was also detected, where the corresponding peaks appear at higher binding energy (0.6 eV for Se 3d and 0.8 eV for Sn 3d) than the SnSe peaks. In addition to the SnSe<sub>x</sub> film, a signal from metallic Se was detected at a binding energy of 54.7 eV, suggesting that some selenium remained unreactive in a metallic form ( $\text{Se}^0$ ).

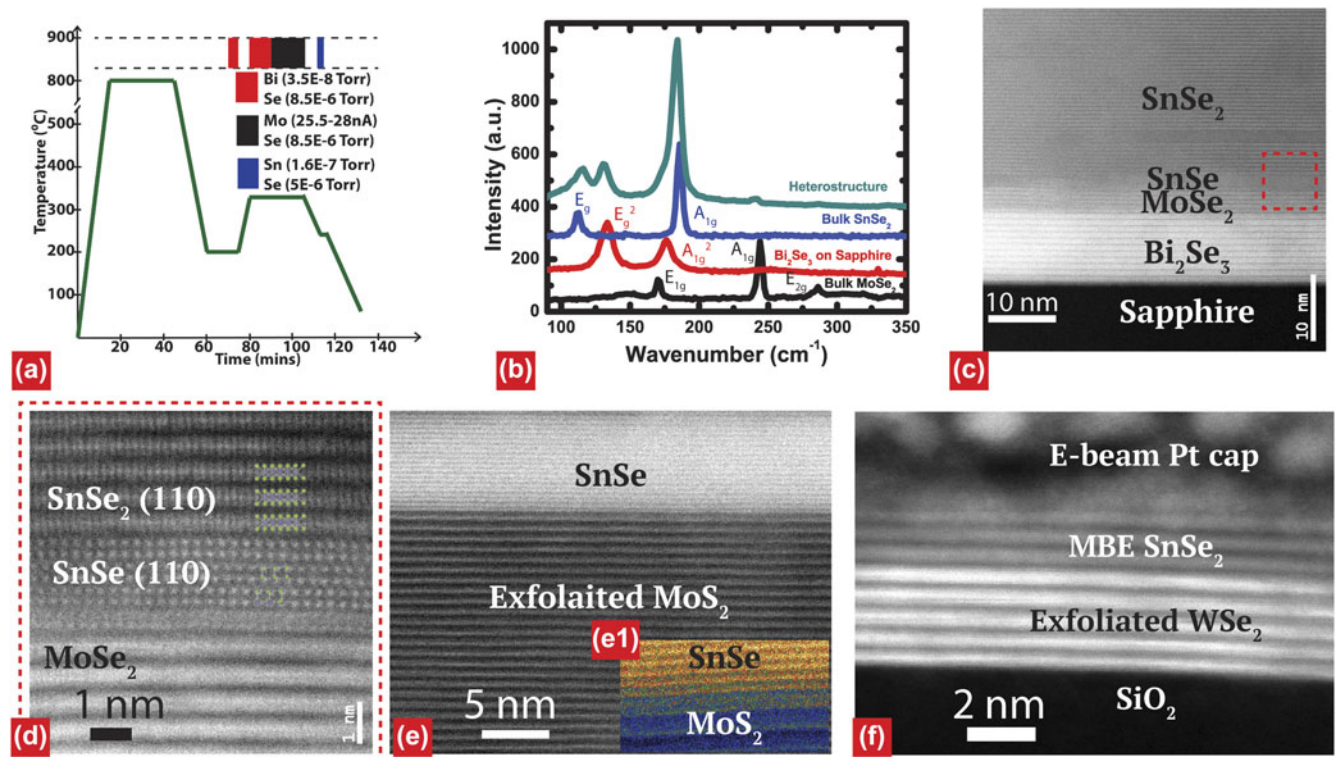


FIG. 6. (a) Growth diagram of the  $\text{Bi}_2\text{Se}_3/\text{MoSe}_2/\text{SnSe}_2$  heterostructure, (b) Raman spectrum from the heterostructure compared to those from MBE grown  $\text{Bi}_2\text{Se}_3$  on sapphire, bulk  $\text{MoSe}_2$  and bulk SnSe<sub>2</sub>, (c) HAADF-STEM image of the heterostructure, (d) higher magnification image of the interface of SnSe<sub>2</sub> on  $\text{MoSe}_2$ , (e) HAADF-STEM image of another MBE sample showing that single phase SnSe can be grown on  $\text{MoS}_2$ , (f) HAADF-STEM image of yet another MBE sample showing that single phase SnSe<sub>2</sub> can be grown on  $\text{WSe}_2$ .

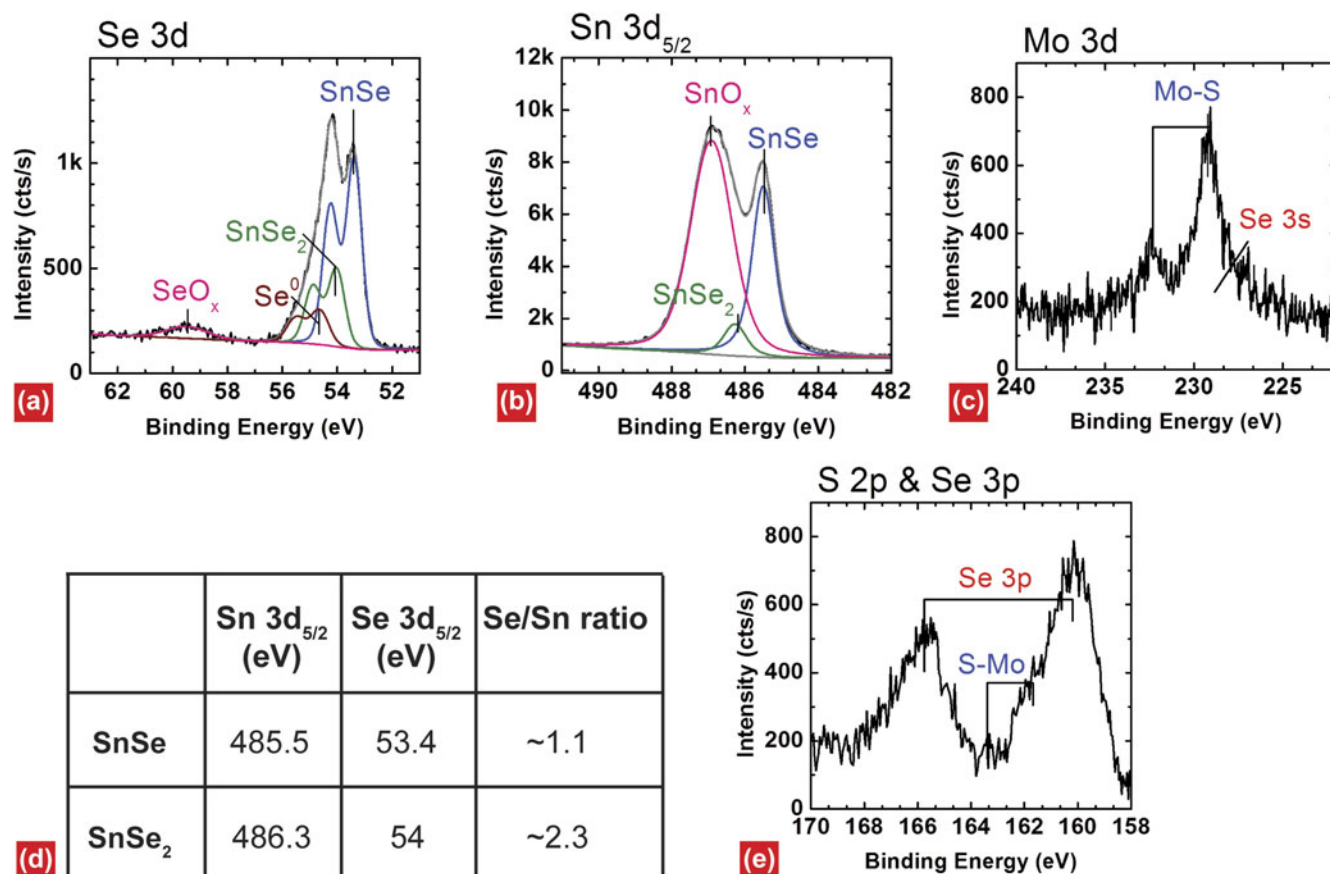


FIG. 7. XPS on sample in Fig. 6(e) (SnSe on exfoliated MoS<sub>2</sub> on SiO<sub>2</sub>/Si) (a) Se 3d core level showing the presence of SnSe, SnSe<sub>2</sub>, metallic Se, and SeO<sub>x</sub>. (b) Sn 3d core level showing the presence of SnSe, SnSe<sub>2</sub>, and SnO<sub>x</sub>. (c and e) low intensity signals from Mo-S bonds are detected, however both Mo 3d and S 2p overlap with selenium related regions from SnSe<sub>x</sub> complicating the deconvolution for MoS<sub>2</sub>, and (d) the stoichiometry for SnSe and SnSe<sub>2</sub> are close to the expected values.

Finally, the presence of surface oxides, SnO<sub>x</sub> and SeO<sub>x</sub>, were also detected in this sample, which could be generated due to air exposure prior to XPS measurements (Fig. 7).

This shows that by optimizing and modeling parameters like growth temperature, interfacial thermal resistance, and the thermal conductivity of the various layers, it is possible to grow single phase SnSe<sub>x</sub> ( $x = 1$  or 2) or a mixed phase with varying concentrations of SnSe<sub>2</sub> and SnSe.

## V. CONCLUSION

In summary, we have demonstrated that MBE is a very unique and powerful tool for growth of layered material heterostructures and SLs. Atomically abrupt MoSe<sub>2</sub>/MoTe<sub>2</sub> SLs with RHEED oscillation for ultrathin layer control have been demonstrated. Heterostructures involving Bi<sub>2</sub>Se<sub>3</sub>, Bi<sub>2</sub>Te<sub>3</sub>, MoSe<sub>2</sub>, SnSe, and SnSe<sub>2</sub> have been grown. Raman and TEM measurements confirm the integrity of the layered materials in these heterostructures. We believe this work serves as a starting point for future optimizations of 2D material MBE heterostructures to

probe theoretical predictions<sup>61–63</sup> of interesting physics in epitaxially aligned heterostructures and SLs.

## VI. INSTRUMENTATION DETAILS

### A. XPS details

XPS was carried out using a monochromated Al K<sub>α</sub> source ( $h\nu = 1486.7$  eV) and an Omicron EA125 hemispherical 7-channel analyzer (Omicron Electronics, Taunusstein, Germany). The XPS scans were acquired at a take-off angle of 45° with respect to the sample normal and pass energy of 15 eV. The software AAnalyzer was used for peak analysis and deconvolution, where Voigt line shapes and an active Shirley background were used for peak fitting.<sup>64</sup>

### ACKNOWLEDGMENTS

L.B. acknowledges the financial support of the National Secretariat of Higher Education, Science, Technology and Innovation of Ecuador (SENESCYT). Microscopy conducted at ORNL's Center for Nanophase

Materials Sciences (CNMS), which is a U.S. Department of Energy, Office of Science User Facility (JCI).

This work was supported in part by the NSF/AFOSR EFRI-2DARE program (1433490), NSF Grant DMR1400432 and Center for Low Energy Systems Technology (LEAST), one of six centers of STARnet, a Semiconductor Research Corporation program sponsored by MARCO and DARPA.

## REFERENCES

1. A.K. Geim and K.S. Novoselov: The rise of graphene. *Nat. Mater.* **6**, 183–191 (2007).
2. B.V. Lotsch: Superlattices of 2D nanosheets. *Annu. Rev. Mater. Res.* **45**(1), 85–109 (2015).
3. F. Wang, Z. Wang, Q. Wang, F. Wang, L. Yin, K. Xu, Y. Huang, and J. He: Synthesis, properties and applications of 2D non-graphene materials. *Nanotechnology* **26**(29), 292001 (2015).
4. S.Z. Butler, S.M. Hollen, L. Cao, Y. Cui, J.A. Gupta, H.R. Gutie, T.F. Heinz, S.S. Hong, J. Huang, A.F. Ismach, E. Johnston-halperin, M. Kuno, V.V. Plashnitsa, R.D. Robinson, R.S. Ruoff, S. Salahuddin, J. Shan, L. Shi, O.M.G. Spencer, M. Terrones, W. Windl, and J.E. Goldberger: Opportunities in two-dimensional materials beyond graphene. *ACS Nano* **7**(4), 2898–2926 (2013).
5. W. Zhao, R.M. Ribeiro, and G. Eda: Electronic structure and optical signatures of semiconducting transition metal dichalcogenide nanosheets. *Acc. Chem. Res.* **48**, 91–99 (2015).
6. Y.S. Hor, A. Richardella, P. Roushan, Y. Xia, J.G. Checkelsky, A. Yazdani, M.Z. Hasan, N.P. Ong, and R.J. Cava: P-type  $\text{Bi}_2\text{Se}_3$  for topological insulator and low-temperature thermoelectric applications. *Phys. Rev. B: Condens. Matter Mater. Phys.* **79** (19), 2–6 (2009).
7. J.E. Boschker, J. Momand, V. Bragaglia, R. Wang, K. Perumal, A. Giussani, B.J. Kooi, H. Riechert, and R. Calarco: Surface reconstruction-induced coincidence lattice formation between two-dimensionally bonded materials and a three-dimensionally bonded substrate. *Nano Lett.* **14**(6), 3534–3538 (2014).
8. S. Das and J. Appenzeller:  $\text{WSe}_2$  field effect transistors with enhanced ambipolar characteristics. *Appl. Phys. Lett.* **103**(10), 103501 (2013).
9. J.S. Ross, P. Klement, A.M. Jones, N.J. Ghimire, J. Yan, D.G. Mandrus, T. Taniguchi, K. Watanabe, K. Kitamura, W. Yao, D.H. Cobden, and X. Xu: Electrically tunable excitonic light-emitting diodes based on monolayer  $\text{WSe}_2$  p-n junctions. *Nat. Nanotechnol.* **9**(4), 268–272 (2014).
10. K. Kim, S. Larentis, B. Fallahzad, K. Lee, J. Xue, D.C. Dillen, C.M. Corbet, and E. Tutuc: Band alignment in  $\text{WSe}_2$  graphene heterostructures. *ACS Nano* **9**(4), 4527–4532 (2015).
11. S.J. Haigh, A. Gholinia, R. Jalil, S. Romani, L. Britnell, D.C. Elias, K.S. Novoselov, L.A. Ponomarenko, A.K. Geim, and R. Gorbachev: Cross-sectional imaging of individual layers and buried interfaces of graphene-based heterostructures and superlattices. *Nat. Mater.* **11**(9), 764–767 (2012).
12. Y. Lin, N. Lu, N. Perea-lopez, J. Li, Z. Lin, X. Peng, C.H. Lee, C. Sun, L. Calderin, P.N. Browning, M.S. Bresnehan, M.J. Kim, T.S. Mayer, M. Terrones, and J.A. Robinson: Direct synthesis of van der Waals solids. *ACS Nano* **8**(4), 3715–3723 (2014).
13. C. Huang, S. Wu, A.M. Sanchez, J.J.P. Peters, R. Beanland, J.S. Ross, P. Rivera, W. Yao, D.H. Cobden, and X. Xu: Lateral heterojunctions within monolayer  $\text{MoSe}_2$ - $\text{WSe}_2$  semiconductors. *Nat. Mater.* **13**, 1096–1101 (2014).
14. J.S. Moon, H. Seo, F. Stratan, M. Antcliffe, A. Schmitz, R.S. Ross, A.A. Kiselev, V.D. Wheeler, L.O. Nyakiti, D.K. Gaskill, K-M. Lee, and P.M. Asbeck: Lateral graphene heterostructure field-effect transistor. *IEEE Electron Device Lett.* **34**(9), 1190–1192 (2013).
15. D. Liang, J.R. Schmidt, and S. Jin: Vertical heterostructures of layered metal chalcogenides by van der Waals epitaxy. *Nano Lett.* **14**(6), 3047–3054 (2014).
16. H. Böttner, G. Chen, and R. Venkatasubramanian: Aspects of thin film superlattice thermoelectric materials, devices, and applications. *MRS Bull.* **31**, 211–217 (2006).
17. H. Osterhage, J. Gooth, B. Hamdou, P. Gwozdz, R. Zierold, and K. Nielsch: Thermoelectric properties of topological insulator  $\text{Bi}_2\text{Te}_3$ ,  $\text{Sb}_2\text{Te}_3$ , and  $\text{Bi}_2\text{Se}_3$  thin film quantum wells. *Appl. Phys. Lett.* **105**(12), 123117 (2014).
18. F.S. Ohuchi, T. Shimada, B.A. Parkinson, K. Ueno, and A. Koma: Growth of  $\text{MoSe}_2$  thin films with Van der Waals epitaxy. *J. Cryst. Growth* **111**, 1033–1037 (1991).
19. F.S. Ohuchi, B.A. Parkinson, K. Ueno, and A. Koma: van der Waals epitaxial growth and characterization of  $\text{MoSe}_2$  thin films on  $\text{SnS}_2$ . *J. Appl. Phys.* **68**(5), 2168 (1990).
20. R. Schlaf, O. Lang, C. Pettenkofer, and W. Jaegermann: Band lineup of layered semiconductor heterointerfaces prepared by van der Waals epitaxy: Charge transfer correction term for the electron affinity rule. *J. Appl. Phys.* **85**(5), 2732 (1999).
21. S. Tiefenbacher, H. Sehnert, C. Pettenkofer, and W. Jaegermann: Epitaxial films of  $\text{WS}_2$  by metal organic van der Waals epitaxy (MO-VDWE). *Surf. Sci.* **318**, L1161–L1164 (1994).
22. C. Hammond, A. Back, M. Lawrence, K. Nebesny, P. Lee, R. Schlaf, and N.R. Armstrong: Growth of layered semiconductors by molecular-beam epitaxy: Formation and characterization of  $\text{GaSe}$ ,  $\text{MoSe}_2$ , and phthalocyanine ultrathin films on sulfur-passivated  $\text{GaP}(111)$ . *J. Vac. Sci. Technol., A* **13**(3), 1768 (1995).
23. T. Hayashi, K. Ueno, K. Saiki, and A. Koma: Investigation of the growth mechanism of an InSe epitaxial layer on a  $\text{MoS}_2$  substrate. *J. Cryst. Growth* **219**, 115–122 (2000).
24. S. Vishwanath, X. Liu, S. Rouvimov, P.C. Mende, A. Azcatl, S. McDonnell, R.M. Wallace, R.M. Feenstra, J.K. Furdyna, D. Jena, and H. Grace Xing: Comprehensive structural and optical characterization of MBE grown  $\text{MoSe}_2$  on graphite,  $\text{CaF}_2$  and graphene. *2D Mater.* **2**(2), 024007 (2015).
25. M.M. Ugeda, A.J. Bradley, S-F. Shi, F.H. da Jornada, Y. Zhang, D.Y. Qiu, W. Ruan, S-K. Mo, Z. Hussain, Z-X. Shen, F. Wang, S.G. Louie, and M.F. Crommie: Giant bandgap renormalization and excitonic effects in a monolayer transition metal dichalcogenide semiconductor. *Nat. Mater.* **13**, 1091–1095 (2014).
26. E. Xenogiannopoulou, P. Tsipas, K.E. Aretouli, D. Tsoutsou, S.A. Giamini, C. Bazioti, G.P. Dimitrakopoulos, P. Kominou, S. Brems, C. Huyghebaert, I.P. Radu, and A. Dimoulas: High-quality large-area  $\text{MoSe}_2$  and  $\text{MoSe}_2/\text{Bi}_2\text{Se}_3$  heterostructures on  $\text{AlN}(0001)/\text{Si}(111)$  substrates by molecular beam epitaxy. *Nanoscale* **7**, 7896–7905 (2015).
27. H. Liu, H. Zheng, F. Yang, L. Jiao, J. Chen, W. Ho, and C. Gao: Line and point defects in  $\text{MoSe}_2$  bilayer studied by scanning tunneling microscopy and spectroscopy. *ACS Nano* **9**(6), 6619–6625 (2015).
28. S-Y. Xu, N. Alidoust, I. Belopolski, A. Richardella, C. Liu, M. Neupane, G. Bian, S-H. Huang, R. Sankar, C. Fang, B. Dellabetta, W. Dai, Q. Li, M.J. Gilbert, F. Chou, N. Samarth, and M.Z. Hasan: Momentum-space imaging of Cooper pairing in a half-Dirac-gas topological superconductor. *Nat. Phys.* **10**, 943–950 (2014).
29. S. Liu, X. Yuan, P. Wang, Z. Chen, L. Tang, E. Zhang, and C. Zhang: Controllable growth of vertical heterostructure  $\text{GaTe}_x\text{Se}_{1-x}/\text{Si}$  by molecular beam epitaxy. *ACS Nano* **9**(8), 8592–8598 (2015).
30. A.K. Geim and I.V. Grigorieva: Van der Waals heterostructures. *Nature* **499**(7459), 419–425 (2013).
31. C. Gong, H. Zhang, W. Wang, L. Colombo, R.M. Wallace, and K. Cho: Band alignment of two-dimensional transition metal

- dichalcogenides: Application in tunnel field effect transistors. *Appl. Phys. Lett.* **103**, 053513 (2013).
32. L.S. McCarthy, I.P. Smorchkova, H. Xing, P. Kozodoy, P. Fini, J. Limb, D.L. Pulfrey, J.S. Speck, M.J.W. Rodwell, S.P. DenBaars, and U.K. Mishra: GaN HBT: Toward an RF device. *IEEE Trans. Electron devices* **48**(3), 543–551 (2001).
  33. H. Kroemer: Heterostructure bipolar transistors and integrated circuits. *Proc. IEEE* **70**, 13–25 (1982).
  34. W.D. Goodhue: Using molecular-beam epitaxy to fabricate quantum-well devices. *Linc. Lab. J.* **2**, 183–205 (1989).
  35. J. Bernède, C. Amory, L. Assmann, and M. Spiesser: X-ray photoelectron spectroscopy study of MoTe<sub>2</sub> single crystals and thin films. *Appl. Surf. Sci.* **219**(3–4), 238–248 (2003).
  36. J.C. Park, S.J. Yun, H. Kim, J. Park, S.H. Chae, S. An, J-G. Kim, S. Kim, K.K. Kim, and Y.H. Lee: Phase-engineered synthesis 2H-molybdenum ditelluride thin films. *ACS Nano* **9**(6), 6548–6554 (2015).
  37. R. Nitsche, H.U. Bolsterli, and M. Lichtenstriger: Crystal growth by chemical transport reactions—I. *J. Phys. Chem. Solids* **21**(3/4), 199–205 (1961).
  38. J.C. Bernede, M. Kettaf, A. Khelil, and M. Spiesser: p-n junctions in molybdenum ditelluride. *Phys. Status Solidi A* **157**, 205–209 (1996).
  39. S. Xiao, M. Li, A. Seabaugh, J. Debdeep, and H.G. Xing: Vertical heterojunction of MoS<sub>2</sub> and WSe<sub>2</sub>. *Device Res. Conf.* **72**, 169–170 (2014).
  40. R. Yan, S. Fathipour, Y. Han, B. Song, S. Xiao, M. Li, N. Ma, V. Protasenko, D.A. Muller, D. Jena, and H.G. Xing: Esaki diodes in van der Waals heterojunctions with broken-gap energy band alignment. *Nano Lett.* **15**(9), 5791–5798 (2015).
  41. M. (Oscar) Li, D. Esseni, G. Snider, D. Jena, and H. Grace Xing: Single particle transport in two-dimensional heterojunction interlayer tunneling field effect transistor. *J. Appl. Phys.* **115**(7), 074508 (2014).
  42. I.G. Lezama, A. Arora, A. Ubaldini, C. Barretero, E. Giannini, M. Potemski, and A.F. Morpurgo: Indirect-to-direct band gap crossover in few-layer MoTe<sub>2</sub>. *Nano Lett.* **15**(4), 2336–2342 (2015).
  43. S. Tongay, H. Sahin, C. Ko, A. Luce, W. Fan, K. Liu, J. Zhou, Y-S. Huang, C-H. Ho, J. Yan, D.F. Ogletree, S. Aloni, J. Ji, S. Li, J. Li, F.M. Peeters, and J. Wu: Monolayer behaviour in bulk ReS<sub>2</sub> due to electronic and vibrational decoupling. *Nat. Commun.* **5**, 3252 (2014).
  44. M. Sugiyama, S. Maeyama, and M. Oshima: Surface-structure analysis of sulfur-passivated GaAs(111)A and GaAs(111)B by x-ray standing-wave triangulation. *Phys. Rev. B* **48**(15), 11037–11042 (1993).
  45. K. Ueno, T. Shimada, K. Saiki, and A. Koma: Heteroepitaxial growth of layered transition metal dichalcogenides on sulfur-terminated GaAs{111} surfaces. *Appl. Phys. Lett.* **56**(4), 327 (1990).
  46. G. Abstreiter, E. Bauser, A. Fischer, and K. Ploog: Raman spectroscopy—A versatile tool for characterization of thin films and heterostructures of GaAs and Al<sub>x</sub>Ga<sub>1-x</sub>As. *Appl. Phys.* **16**(4), 345–352 (1978).
  47. T. Böker, R. Severin, A. Müller, C. Janowitz, R. Manzke, D. Voß, P. Krüger, A. Mazur, and J. Pollmann: Band structure of MoS<sub>2</sub>, MoSe<sub>2</sub>, and α-MoTe<sub>2</sub>: Angle-resolved photoelectron spectroscopy and ab initio calculations. *Phys. Rev. B* **64**(23), 235305 (2001).
  48. X. Liu, D.J. Smith, H. Cao, Y.P. Chen, J. Fan, Y-H. Zhang, R.E. Pimpinella, M. Dobrowolska, and J.K. Furdyna: Characterization of Bi<sub>2</sub>Te<sub>3</sub> and Bi<sub>2</sub>Se<sub>3</sub> topological insulators grown by MBE on (001) GaAs substrates. *J. Vac. Sci. Technol., B* **30**(2), 02B103 (2012).
  49. S. Vishwanath, X. Liu, S. Rouvimov, A. Azcatl, R.M. Wallace, J.K. Furdyna, D. Jena, and H. Grace Xing: MBE growth of MoTe<sub>2</sub>. (2015). In preparation.
  50. R. He, Z. Wang, R.L.J. Qiu, C. Delaney, B. Beck, T.E. Kidd, C.C. Chancey, and X.P.A. Gao: Observation of infrared-active modes in Raman scattering from topological insulator nanoplates. *Nanotechnology* **23**(45), 455703 (2012).
  51. W. Richter, H. Kohler, and C.R. Becker: A raman and far-infrared investigation of phonons in the rhombohedral V<sub>2</sub>–VI<sub>3</sub> compounds Bi<sub>2</sub>Te<sub>3</sub>, Bi<sub>2</sub>Se<sub>3</sub>, Sb<sub>2</sub>Te<sub>3</sub> and Bi<sub>2</sub>(Te<sub>1-x</sub>Se<sub>x</sub>)<sub>3</sub> (0 < x < 1), (Bi<sub>1-y</sub>Sb<sub>y</sub>)<sub>2</sub>Te<sub>3</sub> (0 < y < 1). *Phys. Status Solidi B* **84**, 619–628 (1977).
  52. M. Yamamoto, S.T. Wang, M. Ni, Y.F. Lin, S.L. Li, S. Aikawa, W. Bin Jian, K. Ueno, K. Wakabayashi, and K. Tsukagoshi: Strong enhancement of Raman scattering from a bulk-inactive vibrational mode in few-layer MoTe<sub>2</sub>. *ACS Nano* **8**(4), 3895–3903 (2014).
  53. L-D. Zhao, S-H. Lo, Y. Zhang, H. Sun, G. Tan, C. Uher, C. Wolverton, V.P. Dravid, and M.G. Kanatzidis: Ultralow thermal conductivity and high thermoelectric figure of merit in SnSe crystals. *Nature* **508**(7496), 373–377 (2014).
  54. L. Li, Z. Chen, Y. Hu, X. Wang, T. Zhang, W. Chen, and Q. Wang: Single-layer single-crystalline SnSe nanosheets. *J. Am. Chem. Soc.* **135**(4), 1213–1216 (2013).
  55. T. Shimada, F.S. Ohuchi, and A. Koma: Molecular beam epitaxy of SnSe<sub>2</sub>: Chemistry and electronic properties of interfaces. *Jpn. J. Appl. Phys.* **32**, 1182–1185 (1993).
  56. R. Schlaf, D. Louder, O. Lang, C. Pettenkofer, W. Jaegermann, K.W. Nebesny, P.A. Lee, B.A. Parkinson, and N.R. Armstrong: Molecular beam epitaxy growth of thin films of SnS<sub>2</sub> and SnSe<sub>2</sub> on cleaved mica and the basal planes of single-crystal layered semiconductors: Reflection high-energy electron diffraction, low-energy electron diffraction, photoemission, and scanning tunneling. *J. Vac. Sci. Technol., A* **13**(3), 1761 (1995).
  57. D.G. Mead and J.C. Irwin: Raman spectra of SnS<sub>2</sub> and SnSe<sub>2</sub>. *Solid State Commun.* **20**, 885–887 (1976).
  58. A.J. Smith, P.E. Meek, and W.Y. Liang: Raman scattering studies of SnS<sub>2</sub> and SnSe<sub>2</sub>. *J. Phys. Chem. C* **10**, 1321 (1977).
  59. S. Vishwanath, X. Liu, S. Rouvimov, J.K. Furdyna, D. Jena, and H. Grace Xing: Influence of growth conditions on MBE tin selenide on GaAs (111)B. (2015). In preparation.
  60. N.D. Boscher, C.J. Carmalt, R.G. Palgrave, and I.P. Parkin: Atmospheric pressure chemical vapour deposition of SnSe and SnSe<sub>2</sub> thin films on glass. *Thin Solid Films* **516**, 4750–4757 (2008).
  61. H. Terrones, F. López-Urías, and M. Terrones: Novel hetero-layered materials with tunable direct band gaps by sandwiching different metal disulfides and diselenides. *Sci. Rep.* **3**, 1549 (2013).
  62. G. Gao, W. Gao, E. Cannuccia, J. Taha-Tijerina, L. Balicas, A. Mathkar, T.N. Narayanan, Z. Liu, B.K. Gupta, J. Peng, Y. Yin, A. Rubio, and P.M. Ajayan: Artificially stacked atomic layers: Toward new van der Waals solids. *Nano Lett.* **12**(7), 3518–3525 (2012).
  63. J. He, K. Hummer, and C. Franchini: Stacking effects on the electronic and optical properties of bilayer transition metal dichalcogenides MoS<sub>2</sub>, MoSe<sub>2</sub>, WS<sub>2</sub>, and WSe<sub>2</sub>. *Phys. Rev. B* **89**(7), 075409 (2014).
  64. A. Herrera-Gómez, A. Hegedus, and P.L. Meissner: Chemical depth profile of ultrathin nitrided SiO<sub>2</sub> films. *Appl. Phys. Lett.* **81**(6), 1014–1016 (2002).